Nanostructures of etherified arabinoxylans and the effect of arabinose content on material properties

Carbohydrate Polymers 331 (2024) 121846

Contents lists available at ScienceDirect

Carbohydrate Polymers

journal homepage: www.elsevier.com/locate/carbpol

Nanostructures of etherified arabinoxylans and the effect of arabinose content on material properties

Ratchawit Janewithayapun [a,b], Mikael S. Hedenqvist [b,c,d], Fabrice Cousin [e], Alexander Idström [a], Lars Evenäs [a,b,f], Patricia Lopez-Sanchez [g], Gunnar Westman [a,b,f], Anette Larsson [a,b,f], Anna Ström [a,b,*]

[a] Department of Chemistry and Chemical Engineering, Chalmers University of Technology, SE-412 96 Gothenburg, Sweden
[b] FibRe Center for Lignocellulose-based Thermoplastics, Chalmers University of Technology, SE-412 96 Gothenburg, Sweden
[c] Department of Fibre and Polymer Technology, School of Engineering Science in Chemistry, Biotechnology and Health, KTH Royal Institute of Technology, SE-100 44 Stockholm, Sweden
[d] Wallenberg Wood Science Center, KTH Royal Institute of Technology, SE-100 44, Stockholm, Sweden
[e] Laboratoire Léon Brillouin, Université Paris-Saclay, UMR 12, CEA-CNRS, 91191 Gif Sur Yvette, France
[f] Wallenberg Wood Science Center, Chalmers University of Technology, SE-412 96 Gothenburg, Sweden
[g] Department of Analytical Chemistry, Nutrition, and Food Science. Facultad de Ciencias, Instituto de Materiales (IMATUS), Universidade de Santiago de Compostela, Campus Terra, 27002 Lugo, Spain

ARTICLE INFO

Keywords:
Thermoplasticity
Hemicellulose
Etherification
Oxidation
Mechanical properties
Wheat bran

ABSTRACT

To further our understanding of a thermoplastic arabinoxylan (AX) material obtained through an oxidation-reduction-etherification pathway, the role of the initial arabinose:xylose ratio on the material properties was investigated. Compression molded films with one molar substitution of butyl glycidyl ether (BGE) showed markedly different tensile behaviors. Films made from low arabinose AX were less ductile, while those made from high arabinose AX exhibited elastomer-like behaviors. X-ray scattering confirmed the presence of nano-structure formation resulting in nano-domains rich in either AX or BGE, from side chain grafting. The scattering data showed variations in the presence of ordered structures, nano-domain sizes and their temperature response between AX with different arabinose contents. In dynamic mechanical testing, three transitions were observed at approximately −90 °C, −50 °C and 80 °C, with a correlation between samples with more structured nano-domains and those with higher onset transition temperatures and lower storage modulus decrease. The mechanical properties of the final thermoplastic AX material can therefore be tuned by controlling the composition of the starting material.

1. Introduction

As an abundant polysaccharide in cereals and grasses, arabinoxylan (AX) has potential to replace fossil fuel-based sources for thermoplastic materials. AX is extractable from wheat bran, which is an underutilized waste stream from food production (Prückler et al., 2014). Similar to other plant-based polymers and macromolecules, AX cannot be melt-processed in its native state as the required processing temperatures are higher than their degradation point (Börjesson et al., 2019; Farhat et al., 2018). In order to achieve melt-processability in AX and structurally related wood xylan, strategies to obtain a low glass transition temperature (T_g) have aimed at increasing backbone flexibility via ring-opening oxidation reactions (Amer et al., 2016; Börjesson et al., 2018a; Kristiansen et al., 2010; Palasingh et al., 2022), or at reducing chain-chain polar interactions via grafting reactions (Börjesson et al., 2019; Farhat et al., 2018; Jia et al., 2023).

Previous work has shown that through a sequence of oxidation-reduction-etherification reactions with butyl glycidyl ether (BGE), it is possible to obtain modified AX material with a T_g below 0 °C (Deralia et al., 2021a), thermoplasticity (Börjesson et al., 2019), and a film stretchability above 100 % (Börjesson et al., 2019). The modification route is of particular interest and further studied here as the reactions

* Corresponding author at: Department of Chemistry and Chemical Engineering, Chalmers University of Technology, Kemivägen 10, SE-41296 Gothenburg, Sweden.
E-mail address: anna.strom@chalmers.se (A. Ström).

https://doi.org/10.1016/j.carbpol.2024.121846
Received 16 November 2023; Received in revised form 1 January 2024; Accepted 18 January 2024
Available online 24 January 2024

can be performed effectively with water as solvent, and at temperatures as low as 45 °C (Börjesson et al., 2019; Deralia et al., 2021b), BGE is the preferred ether side chain as glycidyl ethers that are more sterically hindered such as isopropyl glycidyl ether do not react as well, neither do longer chain glycidyl ethers, which are less water soluble such as ethylhexyl glycidyl ether (Deralia et al., 2021b).

Questions remain however, about the mechanisms behind and the dynamics involved in the achieved thermoplasticity and materials properties. Ring-opening oxidation reactions have been shown to lower the persistence length of polysaccharides (Kristiansen et al., 2010), but does not sufficiently reduce T_g to allow for melt processing even at higher degrees of oxidation. Etherification has a more significant impact on melt-processability of the AX material on its own (Börjesson et al., 2018a). A combination of the two, where ring-opening occurs prior to etherification, has shown synergistic effects, resulting in materials with improved processability and ductility at lower BGE content (Börjesson et al., 2019). Films from etherified materials without ring-opening had lower stretchability/ductility by a factor of three to five (Börjesson et al., 2019). Furthermore, achieving thermoplasticity with only etherification required a degree of substitution >3.6 (Deralia et al., 2021a). In which case, it is possible that some BGE were simply blended into the material and not covalently attached. Lastly, it has been observed that the results of the modification depended on the composition of the starting AX material (Börjesson et al., 2018b).

In this work, investigations on the nanostructural changes after modification (etherification and ring-opening) of AX were performed with thermo-mechanical testing, and with X-ray scattering. Our hypothesis is that the arabinose content, and thereby, the branching density of the AX starting materials would result in changes to the final product's thermal relaxations and nanostructure. When the arabinose content of AX decreases, their crystallinity increases (Heikkinen et al., 2013). The ordered regions are expected to carry over to the final material, resulting in higher stiffness and brittleness. Furthermore, branching and the entanglements occurring as a result are also major considerations for polymers (Landel & Nielsen, 1993). Therefore, the branching density controlled by the arabinose content should also play a role in the properties of modified AX. Beiner and Huth (2003) showed on branched poly(n-alkyl methacrylate)s that immiscible alkyl side chains result in separation into nano-domains, leading to two dynamics occurring simultaneously within the system: mobile side chain domains, and a rigid main chain separating the domains. Similar phase separations were observed in alkyl substituted cellulose (Chen et al., 2014; Crépy et al., 2011), and alkyl substituted chitosan (Liu et al., 2020). We expect that such nano-domains would also exist in an AX-BGE system and are interested in investigating the effects of the AX composition on the side chain and main chain motions.

To obtain AX with differing arabinose:xylose (ara:xyl) ratios, we use ethanol (EtOH) fractionation on wheat bran extracted AX – allowing for a study of AX from the same source material, which has not previously been done. The degree of etherification was controlled at 1.0 molar substitution (MS), and diffusion NMR was used to confirm the removal of non-bound BGE. By adjusting the ara:xyl ratio, the resulting film exhibits a range of properties; transitioning from a rather non-ductile material to a ductile plastic, and ultimately to a material with tensile properties more akin to an elastomer.

2. Experimental

2.1. Materials

The wheat bran was kindly provided by Lantmännen. The bran was then milled and sieved through a 1 mm mesh. Chemicals used for the extraction: hydrochloric acid, sodium chlorite ($NaClO_2$), sodium hydroxide, sodium dithionite ($Na_2S_2O_4$) were purchased from Sigma-Aldrich (Schnelldorf, Germany). Ethanol (95 %) was purchased from Solveco (Rosersberg, Sweden). α-amylase from *Bacillus Licheniformis* >500 units/mg protein was purchased from Sigma-Aldrich (Schnelldorf, Germany) and β-glucanase (EC.2.1.73) from *Bacillus Subtilis* was purchased from Megazyme (Wicklow, Ireland). Chemicals used for the oxidation, reduction, and etherification reactions: sodium periodate ($NaIO_4$), sodium borohydride ($NaBH_4$), sodium phosphate monobasic (NaH_2PO_4), butyl glycidyl ether (BGE) were purchased from Sigma-Aldrich (Schnelldorf, Germany). The chemicals were used without further purification. Deionized (DI) water was used throughout the experiments. Regenerated cellulose dialysis membrane (Spectra/Por 3) with a molecular weight cutoff of 3.5 kDa was purchased from Spectrum Laboratories (Rancho Dominguez, CA).

2.2. Isolation of arabinoxylan

AX was isolated from wheat bran on a 1 kg scale using an alkaline extraction process described in earlier work (Börjesson et al., 2018a; Börjesson et al., 2019). In brief, wheat bran was pre-treated in acid, delignified with $NaClO_2$, and AX was extracted under alkaline conditions with $Na_2S_2O_4$ as a reducing agent. A similar method to those previously reported for rye and wheat grain (De Man et al., 2021) (Scheme 1) was used for precipitation and fractionation of AX with different arabinose content. The extracted dispersion containing AX was first concentrated to half-volume in a rotary evaporator at 60 °C and pressure < 70 mbar. Fractionation via sequential precipitation in increasing concentrations of ethanol (EtOH) followed (20, 40, 60 and 80 % *v*/v). The precipitate was then recovered by centrifugation (Heraeus Megafuge 40, Thermo Scientific, 4500 rpm, 15 min), and dialyzed against DI water through a dialysis membrane (3.5 kDa cutoff) until a conductivity below 5 μS was reached.

5 g of the fraction from 20 %v/v, from here on referred to as AX0.3, from its ara:xyl ratio, (5 g), was dispersed in sodium phosphate buffer (200 ml, 20 mM, pH 6.5). β-glucanase solution (500 μL, 25 units) was added. The contents were stirred with a magnetic stirrer at 50 °C overnight. AX0.3 was recovered by precipitation in EtOH (400 ml, final EtOH concentration 66 %) followed by centrifugation. In addition to fraction AX0.3, the fractions extracted at 60 % v/v and 80 % v/v were chosen for further chemical modification to obtain a range of ara:xyl ratio for comparative studies. These were named AX0.5 and AX0.9, respectively, from their ara:xyl ratios.

2.3. Periodate oxidation and sodium borohydride reduction of AX

Periodate oxidation was performed to achieve ring-opening oxidation of AX as previously described (Amer et al., 2016;Börjesson et al., 2018a ; Börjesson et al., 2019). All molar equivalents are based on one anhydroxylose (AXU) having an average molecular weight of 132.1 g/mol. Freeze-dried AX (2 g, 15.14 mmol AXU) was ground with a mortar and pestle until a fine powder was obtained. The AX was stirred vigorously in DI water (82.5 ml) at 70 °C until dispersion was achieved.

Based on previous studies (Börjesson et al., 2018a; Börjesson et al., 2019), $NaIO_4$ (0.810 g, 3.8 mmol, 0.25 equiv.) was added to the AX dispersions to obtain a degree of oxidation (DO) of approximately 20 %. The $NaIO_4$ was first dissolved in DI water (12.5 ml), then added to the AX dispersion. The concentration of AX in the final mixture was 2 wt%. The reaction flask was protected from light and stirred at room temperature for 17 h.

The dialdehyde groups were reduced into dialcohol groups as follows: $NaBH_4$ (1 g, 26.43 mmol, 1.75 equiv.) and NaH_2PO_4 (0.15 g) were dissolved in DI water (25 ml), then added to the oxidized AX dispersion. The reduction was performed with stirring for 4 h at room temperature. (Börjesson et al., 2019; Larsson et al., 2014) The samples were then purified through dialysis against DI water for two days with repeated changes of water (Palasingh et al., 2022). After dialysis, samples were collected and stored at 4 °C. The oxidized and reduced AX material with dialcohol groups were designated DiolAX.

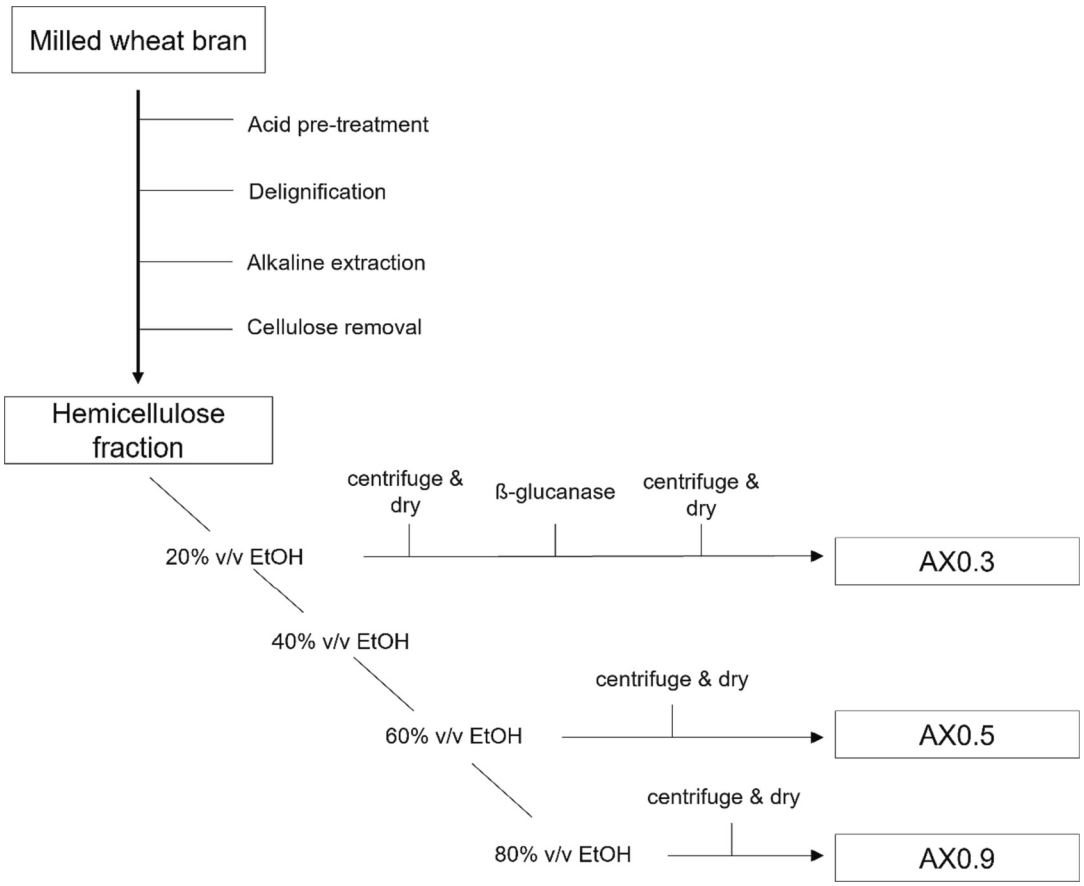

Scheme 1. Fractionation of wheat bran AX through precipitation in increasing concentrations of ethanol. The fraction from 20 % v/v EtOH precipitation was further purified to remove β-glucan which co-precipitated with the other insoluble compounds during centrifugation.

2.4. Etherification of DiolAX

DiolAX was grafted with BGE following the method described by Nypelö et al. (2016) and later Börjesson et al. (2019) with minor modifications. The DiolAX solution from the previous step was reduced in volume on a rotary evaporator, resulting in a concentration of ca. 4 % AX in water (). NaOH (1.82 g, 45.5 mmol, 3 equiv.) was added to the 4 % AX in a 250 ml three-necked round-bottom flask equipped with a reflux condenser and nitrogen inlet. Then, BGE (5.92 g, 45.5 mmol, 3 equiv.), in a 1:1 molar ratio with NaOH, was slowly added to the solution through a needle over 30 min. The mixture was stirred overnight at 45 °C. After the reaction, the solutions were neutralized with 1 M H_2SO_4 and dialyzed against DI water for two days with repeated changes of water. The BGE modified DiolAX was recovered from the dialysis through centrifugation and air-dried in a convection oven at 30 °C. These samples are referred to as BGE-DiolAX.

2.5. Preparation of films

The films were prepared by compression molding. The dried samples were weighed into a mold with dimensions 50 mm × 50 mm × 0.1 mm and pressed between woven Teflon sheets supported by two metal plates at 140 °C for 1 min without force to soften the samples, and then kept at 140 °C for 3 min under 50 kN force. The mold was then removed, metal blocks placed over to maintain compression, and allowed to cool overnight at room temperature.

2.6. Characterization

2.6.1. Monosaccharide composition

The monosaccharide composition was determined by means of high-performance anion exchange chromatography with pulsed amperometric detection (HPAEC-PAD), using an ion chromatography system ICS 3000 (Dionex, Thermo Fisher Scientific) equipped with a CarboPac PA1 (4 × 250 mm^2) analytical column. Samples were hydrolyzed with 72 % sulfuric acid and diluted to 200 mg/L prior to analysis (Sluiter et al., 2008; Theander & Westerlund, 1986). Monosaccharide standards for arabinose, xylose, rhamnose, galactose, glucose and mannose were used for calibration. Milli-Q (MQ) water was used as the eluent at a flowrate of 0.26 ml/min. A mixture of 60 % *v*/v 200 mM NaOH and 40 % v/v 200 mM NaOH with 170 mM NaOAc was run for cleaning between injections. An isocratic flow of 200 mM NaOH solution at a flowrate of 0.13 ml/min was added post-column prior to the detector chamber.

The acid soluble lignin content (ASL) was calculated from the UV absorbance of hydrolysates at 205 nm using the Specord 205 (Analytik Jena, Jena, Germany) (Jedvert et al., 2012). The insoluble content was measured from the weight of dried (overnight at 105 °C) residues after filtration of hydrolysates.

The content of mixed-linkage-β-glucan was measured using the Megazyme mixed-linkage β-glucan assay kit (AOAC Method 995.16, Megazyme International, Wicklow, Ireland).

2.6.2. Molar mass determination

The molar mass distribution of unmodified and modified AX was measured using gel permeation chromatography (PL-HPC 50 Plus Integrated GPC system, Polymer Laboratories, Varian Inc.), equipped with

two 300 × 7.5 mm PolarGel-M columns and one 50 × 7.5 mm PolarGel-M guard column. The mobile phase was dimethyl sulphoxide (DMSO) with 10 mM LiBr at a flow rate of 0.5 ml/min at 50 °C. Detection was made using a refractive index (RI) detector. Calibration was performed with 10 pullulan standards ranging from 0.180 to 708 kDa (Varian PL2090–0100, Varian Inc).

10 mg of each sample was stirred in 1 ml of the mobile phase at 50 °C for 1 h, then overnight at room temperature for dissolution. These were then diluted to a concentration of 2 mg/ml and filtered through 0.2 μm syringe filters. Each sample was run in duplicate. Analysis of data was made with the Cirrus GPC Software 3.2.

2.6.3. Degree of oxidation (DO)

The progress of the oxidation reaction was followed with ultraviolet spectroscopy (Cary 60 UV–Vis, Agilent technologies, Santa Clara, CA, USA) by studying the absorption band at λ = 290 nm corresponding to the concentration of IO_4^- (Maekawa et al., 1986). A linear standard curve for the periodate solution at λ = 290 nm was obtained using concentrations of $NaIO_4$ between 0.1 and 5 mM.

2.6.4. Fourier-transform infrared spectroscopy (FTIR)

The AX samples were analyzed before and after chemical modification using an FTIR spectrophotometer (Frontier, PerkinElmer, Waltham, MA, USA) in attenuated total reflection (ATR) mode in the spectral range of 4000–400 cm^{-1} at room temperature. Spectra were obtained with 4 cm^{-1} resolution and using 16 scans for each spectrum. Measurements were made in duplicates.

2.6.5. Nuclear magnetic resonance (NMR)

The MS was evaluated using NMR spectroscopy as previously described (Börjesson et al., 2019; Theander & Westerlund, 1986). 25 ml of undiluted hydrolysate from the HPAEC sample preparation method were neutralized with $CaCO_3$. Solutions were left to settle, then freeze-dried. The dried solids were dissolved in D_2O and filtered through a 0.2 μm filter to remove remaining $CaCO_3$.

^1H NMR spectra were recorded on a Varian MR-400 MHz spectrometer. D_2O (with residual 1H signal at 4.63 ppm) was used for lock and chemical shift calibration. MS was calculated from Eq. (1), where the integral intensity from the signal from the BGE methyl group signal (0.9 ppm) was compared to the signals of α-H1 (5.2 ppm) and β-H1 (4.5 ppm) from the AX units.

$$MS = \frac{\int(3\ methyl\ protons\ of\ BGE)}{3\ x\ \left(\int \alpha H1 + \int \beta H1\right)} \quad (1)$$

For pulsed-field gradient diffusion NMR measurements, samples of BGE-diol AX, obtained after dialysis and subsequent drying, were dissolved in DMSO-d_6. Measurements were conducted on a Varian Inova 500 MHz operating at 11.7 T with a 5 mm HFX-probe, with magnetic field gradients up to 60 G/cm. The DgcsteSL (DOSY Gradient Compensated Stimulated Echo with Spin Lock) sequence was used with parameters including an 8.8 μs 90° ^1H-pulse, 4 s acquisition time, 2 s recycle delay, 128 scans per point, gradient pulse length δ of 8 ms, and diffusion time Δ of 200 ms. Gradients g ranging from 0.18 to 60 G/cm were used in 16 steps. The chemical shifts were calibrated using the DMSO signal at 2.50 ppm. Gradient strengths were calibrated against residual ^1H water signal in pure D_2O (self-diffusion coefficient 1.902×10^{-9} m^2/s at 298 K). Mestrenova 14.1.2 was used to process the data and the self-diffusion coefficients were calculated by regression analysis using Matlab software program.

The intensities of the assigned signals were plotted against k, seen in Eq. (2).

$$k = (\Delta - \delta/3)^*(\delta^*\gamma^*g)^2 \quad (2)$$

where Δ is the diffusion delay, δ the gradient pulse duration, γ the gyromagnetic ratio of the nucleus studied, and g the gradient strength. For non-overlapping signals, the diffusion coefficients were calculated from least squares fitting of the attenuation curves, using Eq. (3).

$$I(k) = I_0\ exp(-kD) \quad (3)$$

where $I(k)$ is the intensity of the signal at a certain k, I_0 is the intensity at the first k, and D is the diffusion coefficient. For overlapping signals with a big difference between the self-diffusion coefficients, Eq. (4) was used.

$$I(k) = I_{0,f}\ exp\left(-kD_f\right) + I_{0,s}exp(-kD_s) \quad (4)$$

where f and s denote fast and slow diffusing species, respectively. The obtained diffusion coefficients were calibrated against a reference water signal in D_2O (1.902×10^{-9} m^2/s at 298 K).

2.6.6. Tensile testing

Film samples were conditioned in a climate room at 23 ± 1 °C at 50 ± 2.5 % relative humidity (RH) for over 72 h before testing. Measurements were conducted in the same climate using a 5944 Universal Tensile Testing machine (MA, USA) in accordance with ASTM D882. At least 5 replicates were tested for each sample. Straight rectangular specimens were cut out from sample sheets, having a cross-section of 2 × 0.1 mm^2 and a length of 30 mm. A gauge length of 15 mm was used. The thickness of samples varied slightly for each batch and were measured individually with a micrometer. A preload of 0.05 N and crosshead speed of 30 mm/min were used.

2.6.7. Thermal properties

Dynamic mechanical properties were measured on a Q800 DMA (TA Instruments, U.S.) in film tension mode. The sample size was approximately 30 mm × 10 mm × 0.15 mm. The sample width and thickness were measured with a micrometer and caliper prior to measurements. The length used in calculations was taken from the gauge measured by the instrument.

For temperature sweep experiments, the samples were equilibrated at −130 °C for 5 min. Then, measurements were made with a heating rate of 3 °C/min, frequency of 1 Hz and an amplitude of 8 μm. Samples were conditioned in a climate chamber at 25 °C and 55 % relative humidity for at least 24 h before measurements.

Differential scanning calorimetry (DSC) was measured using a DSC 2 STARe system (Mettler Toledo, Switzerland), under N_2 flow of 50 ml/min. Samples were equilibrated at −80 °C for 5 min and then heated to 170 °C at a rate of 20 °C/min. A cooling and a second heating cycle followed – cooling to −80 °C at 20 °C/min, then to 170 °C at 20 °C/min.

2.6.8. Pycnometry

The density of AX0.3 and BGE-diol AX0.3 was determined using an AccuPyc II 1340 gas pycnometer (Micromeritics) in a 10 cm^3 cylindrical holder under helium flow. Calibration against metal beads with known density was performed. Five purging and analysis cycles were performed for each sample.

2.6.9. X-ray scattering

Small-angle (SAXS) and wide-angle (WAXS) X-ray scattering measurements were conducted on a SAXSLAB Mat:Nordic (Denmark) benchtop instrument with a Cu Kα radiation source, covering a Q range from 0.01 to 2.7 $Å^{-1}$. The detector distance was 477 mm and 126 mm for SAXS and WAXS, respectively. Q-calibration was performed using silver behenate powder. Modified BGE-DiolAX samples were mounted between two Kapton films and clamped to a solid sample holder, while the AX0.9 sample was solvent casted and measured as a self-standing film.

For temperature step SAXS experiments, the BGE-diol AX films were placed between Kapton films to reduce warpage and secured onto a Linkam300 heating stage. An external thermocouple was secured to measure the temperature of the surface of the film in addition to the temperature of the heating stage. 12 temperature settings were used

between 25 °C and 200 °C, corresponding to 25 °C to 120 °C on the sample surface. Each sample was equilibrated for 15 min at each temperature before measurement with 600 s exposure time.

For both measurement methods, the direct beam intensity was measured to determine the absolute intensity of the measured scattering patterns. Data reduction was done with the SAXSGUI software (version 2.27.03). Thickness correction and subtraction of the Kapton background were done using Matlab software program. Peak fitting to various lineshapes were performed using the Fityk software (version 1.3.1).

XRD measurements were conducted on a Bruker D8 Discover, instrument using a Bragg-Brentano setup with Cu Kα radiation source, covering 2θ from 5°-60° (Q range 0.35–4.08 $Å^{-1}$). Film samples were mounted onto a single crystal Si holder. Measurements were analyzed using DIFFRAC.EVA software (version 6.0).

3. Results and discussion

3.1. Composition of AX fractions

The monosaccharide composition (Table 1) show that the extracted material was predominantly composed of AX, and the ara:xyl ratio increases with EtOH concentration in agreement with previous studies of AX from rye and wheat grain (Maes & Delcour, 2002; Verwimp et al., 2007). Also observed, was that the fraction denoted AX0.3 contained a larger content of glucose and precipitated non-water-soluble materials compared to the other two samples. The majority of glucose content in AX0.3 was β-glucans, accounting for 14 wt% of the material. As such, further purification using β-glucanase, to reduce the glucose content was performed. The purified AX0.3 showed a lower amount of glucose, indicating that ß-glucan had co-precipitated during the fractionation. The purification and reprecipitation further lowered the ara:xyl ratio in AX0.3. The major compositional difference (apart from arabinose and xylose) between the samples (AX0.3, AX0.5 and AX0.9) is the amount of insolubles of AX0.3 (15 wt%) compared to AX 0.5 and AX 0.9 (4 and 5 wt % respectively). Insolubles here include lignin that is not soluble under acid conditions (ASL), but also other compounds that were not hydrolyzed. The relatively higher percentage of insolubles, as observed in the starting material AX0.3, does not carry over to the modified sample. The modification, and dialysis process resulted in modified samples from all AX samples with insoluble contents between 3.7 and 4.9 wt% (Table S1). In addition, insolubles are not expected to influence material properties, which should be dominated by polymeric materials susceptible to acid hydrolysis.

3.2. Results of periodate oxidation, reduction and BGE substitution

The degree of oxidation, (DO), was determined via the absorption band in UV–Vis at 290 nm. 100 %, 84 % and 88 % of added sodium periodate were consumed for AX0.3, AX0.5 and AX0.9, respectively. These corresponded to DO of 25 %, 21 % and 22 %. For the oxidation of the AX0.3, the UV spectra pattern changes to a larger extent with reaction time due to scattering from dispersed AX0.3 or dialdehyde AX0.3 aggregates. This resulted in calculated consumption values >100 %, which was assumed as complete oxidation and reported as a DO of 25 %. Nevertheless, our results are aligned with a DO of around 20 %, which was expected based on previous work in which different periodate concentrations were used (Börjesson et al., 2018a).

Table 1
Monosaccharide composition in wt%, mass of insolubles and acid soluble lignin (ASL) of AX0.3 before and after addition of ß -glucanase, AX0.5 and AX0.9. n.d. – not detected, below detection limit of method.

Component (wt%)	AX0.3 (before ß-glucanase)	AX0.3	AX0.5	AX0.9
Arabinose	23	17	29	41
Rhamnose	n.d.	n.d.	n.d.	n.d.
Galactose	2	1	3	3
Glucose	15	8	8	3
Xylose	41	56	53	44
Mannose	n.d.	n.d.	n.d.	n.d.
Insolubles	11	15	4	5
ASL	9	3	3	4
ara:xyl ratio	0.56	0.30	0.55	0.93

The samples before and after oxidation/etherification were analyzed with FTIR (Fig. S1), to study the introduction of BGE to the AX samples as in previous work (Börjesson et al., 2019). In the butylated samples, the absorption band around 3400 cm^{-1}, corresponding to O—H interactions, has been shifted to higher wavenumbers compared to native samples. The absorption band at 3000–2800 cm^{-1}, showed higher intensity in the butylated samples, indicating an increase in the number of -CH_2 and -CH_3 groups. A decrease of the band at 1630 at cm^{-1} was interpreted as a decrease in hydrated water signals according to a work by Nylander et al. (2019). A stronger absorption band was also observed at 1465 cm^{-1} (CH_2- bending), relative to the unmodified samples. FTIR data indicated that the substitution did take place and the spectra of the butylated samples were similar to those that we previously reported (Börjesson et al., 2019).

Further characterization was performed using the same HPAEC method as monosaccharide characterization (Table 2). Oxidized AX units, and BGE side chain byproducts are not detected by the HPAEC method. It is assumed that all the BGE side groups are cleaved off the AX by hydrolysis. Hence, the mass recovery from HPAEC can be used to estimate the percentage of non-oxidized AX, and the BGE content in BGE-diol AX samples (Table 2). The results indicated that all three samples were similar in the content of unmodified AX, with a slight decrease in unmodified content at higher ara:xyl ratios.

Changes in the ara:xyl ratio after modification are also an indication of the relative reactivities of arabinose and xylose to oxidation (Table 2). Arabinose was consumed to a higher degree than xylose – likely due to the higher accessibility of the OH groups on the arabinose side chain. In the BGE-diol AX0.3 and 0.5, nearly all arabinose was consumed, leading to a decrease of ara:xyl ratio to 0.1 for both. In BGE-diol AX0.9, a decrease in ara:xyl ratio to <0.5 was expected. This was not the case, as the ara:xyl ratio had only decreased to 0.7. A possible explanation could be that a larger number of the arabinose groups are di-substitutions (De Man et al., 2021), and have lower reactivity due to higher steric hindrances between two neighboring arabinose groups. This resulted in oxidation happening to more similar degrees on arabinose and xylose units.

The MS of BGE was calculated from the ^1H NMR spectra of acid hydrolyzed BGE-diol AX samples. Results showed MS close to one for all samples (Table 2), which was in good agreement with the detected unmodified AX content from HPAEC. In addition, we also observed the same trend of increasing modification at higher ara:xyl ratios.

Using the ara:xyl ratio data from Table 1, and MS data from Table 2, an approximation of the distributions of arabinose and BGE side chain substitutions for each BGE-diol AX is shown in Fig. 1. One arabinose unit in AX has three hydroxyl groups which could react, while for non-reducing end xylose in AX, it is two minus any arabinose substitutions present. Assumptions were made that a tri-substitution of BGE on AX would be less sterically favorable and less frequent, and that BGE oligomeric side reactions are suppressed by pre-mixing the diol-AX mixture with NaOH before dosing in BGE. The activated hydroxyl groups on AX were therefore assumed to be more active than hydroxyl groups on the BGE side chains.

The weight averaged molar masses (M_w) of the BGE-diol AX samples were in similar ranges with the unmodified AX for AX0.3 and AX0.5 at M_w of 1.4 and 1.6 × 10^5 g/mol respectively (Table 2). The highest arabinose containing AX0.9 had a larger M_w reduction after modification (3.3 × 10^5 g/mol to 2.6 × 10^5 g/mol) compared to the other two fractions. The dispersity (M_w/M_n) had decreased for AX0.3 and AX0.5 – as the distribution is narrower in both the low and high M_w region

Table 2
Data on composition of modified BGE-diol AX materials including: ara:xyl ratio before and after modification, Unmodified AX content in wt%, MS measured by ^{1}H NMR of hydrolysates, and weight averaged molar mass (M_w) and dispersity (M_w/M_n) measured by GPC.

Material	Ara:xyl ratio before modification	Ara:xyl ratio after modification	Unmodified AX by HPAEC (wt%)	MS by ^{1}H NMR	M_w before modification ($/10^{-5}$ g/mol)	M_w/M_n before modification	M_w after modification ($/10^{-5}$ g/mol)	M_w/M_n after modification
BGE-diol AX0.3	0.3	0.1	43	0.92	1.4	4.0	1.2	2.9
BGE-diol AX0.5	0.5	0.1	38	0.95	1.6	3.6	1.3	2.3
BGE-diol AX0.9	0.9	0.7	35	1.10	3.3	2.3	2.6	3.0

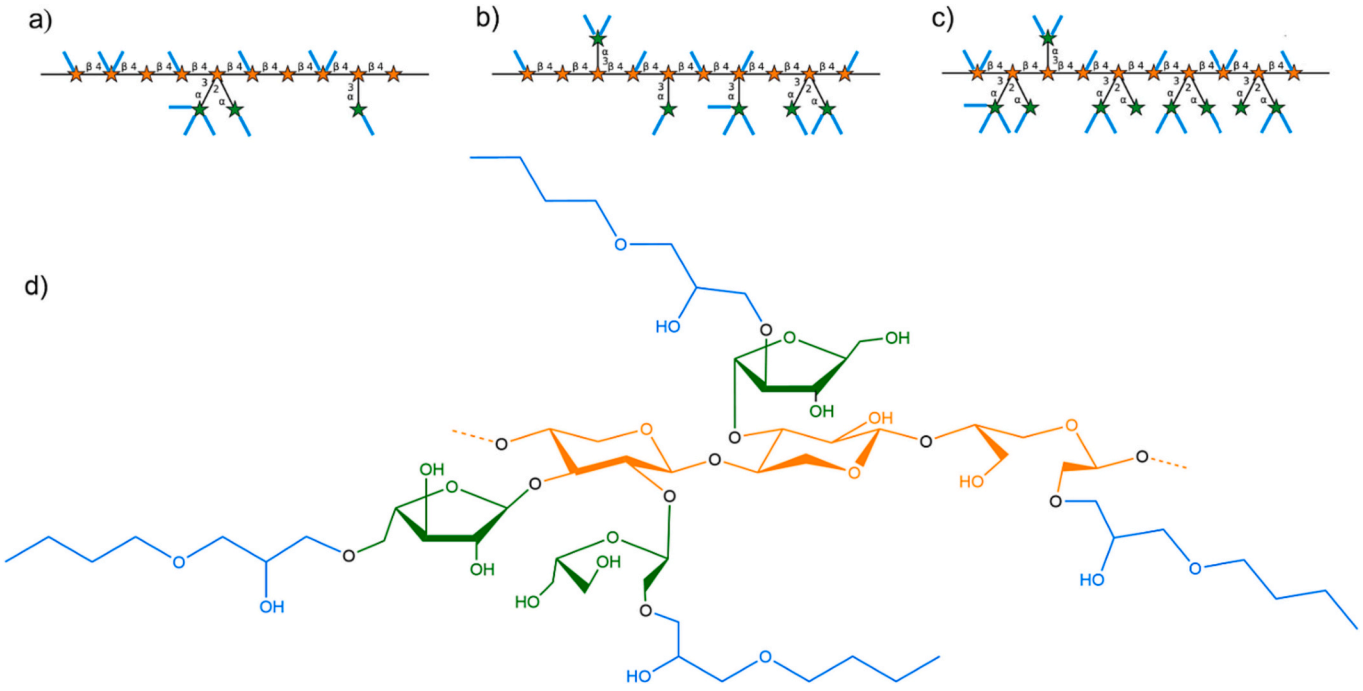

Fig. 1. Illustration of the distributions of arabinose and butyl glycidyl ether (BGE) side chain substitutions in AX based on data presented in Tables 1 and 2, partially drawn using DrawGlycan (Cheng et al., 2016). Orange stars – xylose units, green stars – arabinose units, blue lines – BGE side chains: a) shows BGE-diol AX0.3, b) BGE-diol AX0.5, c) BGE-diol AX0.9, and d) a schematic sketch of the chemical structure of BGE-diol AX with the same colour scheme as in a-c).

(Fig. S2). While for AX0.9, there was an increase of the population with M_w between 10,000–40,000 g/mol, leading to increased dispersity (Fig. S2). The overall shape of the M_w distribution curve remains similar after modification for all AX samples, with the large peaks centered around similar retention times. The M_w values and the distribution curves indicate there was no major degradation of the AX owing to oxidation, and reduction. However, an exact comparison is not possible given the expected differences in solution conformation between AX samples with different branching ratios (Nypelö et al., 2022; Petermann et al., 2023).

The content of BGE added to the material, whether covalently bonded or mixed, strongly affects the mechanical properties of the final material. Therefore, in addition to controlling the MS close to one, in comparison to 3–5 as obtained by Börjesson et al. (2019), pulsed-field gradient diffusion NMR was used to confirm the absence of freely diffusing BGE molecules. The data from the diffusion experiments of the BGE-diol AX0.5 sample can be seen in Fig. 2. In a), a series of DgcsteSL spectra with increasing k is shown. Plotting the log of the signal integral intensities for each spectrum against the k-value produces the figure in b). Fitting the data against a single or, as for the signals with overlapping species, double exponential decay, as described earlier, the self-diffusion coefficient, D, was extracted.

The diffusion of a molecule can be described by the Stokes-Einstein equation, which models a sphere with stick boundary condition at infinite dilution provided by Eq. (5) as

$$D = \frac{k_B T}{6\pi\eta R} \tag{5}$$

where k_B is the Boltzmann constant, T the absolute temperature, η the viscosity of the solvent, and R the hydrodynamic radius of the molecule. A large polymer, with a large R, such as AX, generally have slow diffusivity, whereas a solvent molecule or smaller molecule, such as unreacted BGE, have high diffusivity. Fig. 2b) shows that the slope of the attenuation for all ingoing components, except for faster moving water and DMSO, followed the same decay. This implied that all components have identical or similar self-diffusion coefficients, and therefore, a successful reaction between the AX and BGE with low or no unreacted BGE left in the sample. Measurements on BGE undialyzed samples were performed (Fig. S3) and a mix of slow and fast-diffusing behavior was clearly seen. The possibility of physical absorption of BGE to AX is, therefore, unlikely.

3.3. Compression molded films from BGE-diol AX

BGE-diol AX0.3, 0.5 and 0.9 were compression molded into films of 0.1 mm in thickness. The BGE-diol AX0.3 showed macroscopic

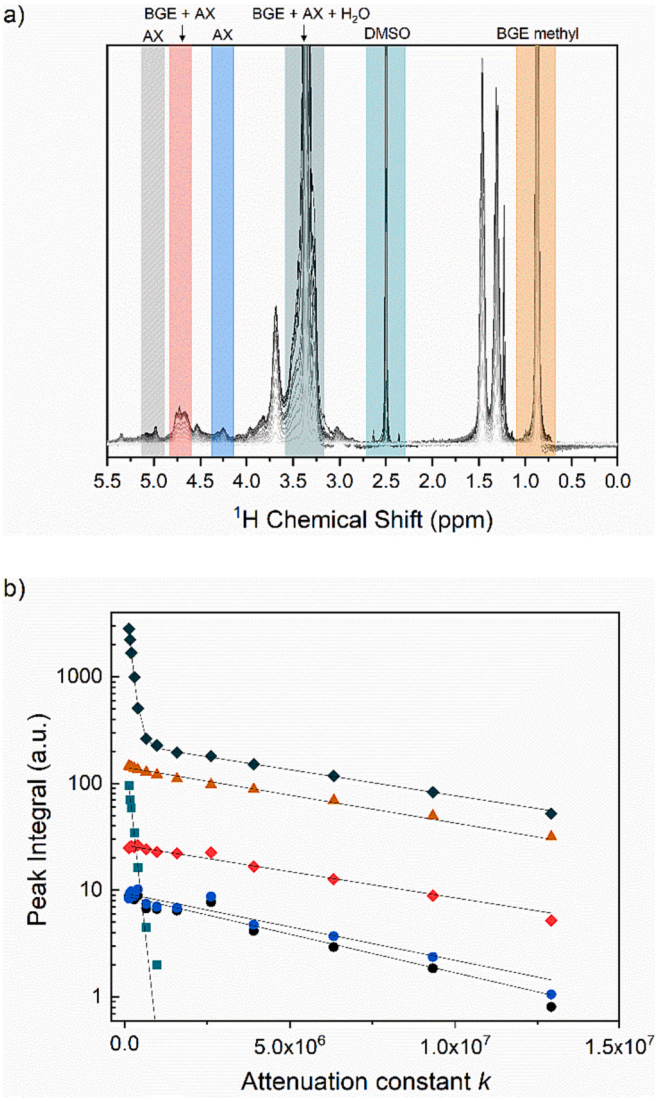

Fig. 2. a) A series of DgcsteSL spectra with increasing *k* of the BGE-diol AX0.5 sample. Signal integral intensities used to follow the attenuation with increased *k* are highlighted and labeled. B) The integral intensity of the following signals plotted against the *k*-value: mixture of BGE, AX sugar ring signals and water (dark green, diamonds), BGE methyl (orange, triangles), DMSO (green, squares), mixture of BGE and AX (overlapped parts of α ara—H1) (red, diamonds), AX ß xyl-H1 (blue, circles), and AX α ara-H1 (black, circles). Lines denote fitting of single- or bi-exponential decays.

inhomogeneities, observed as opaque clusters on the film (Fig. 3a), while the films produced using BGE-diol AX0.5 and BGE-diol AX0.9 were clear and transparent (Fig. 3b–c). When heated to around 85 °C on a Kofler bench, the large opaque clusters on BGE-diol AX0.3 disappear almost completely, but the film still has an inhomogeneous, macroscopically phase separated appearance. It should be noted that the textures observed on all films are a result of patterns on the Teflon sheet. All three films were flexible and could be bent and folded.

3.4. Tensile properties

The compression molded BGE-diol AX films were tensile tested, as well as solvent casted films of AX0.9, the latter serving as a reference of unmodified material. The AX0.9 behaved as a brittle material and showed no significant plastic deformation (Fig. S4), in agreement with previous findings (Börjesson et al., 2019). The mean Young's modulus for AX0.9 was 4720 MPa compared to 111 MPa for BGE-diol AX0.9, and the mean strain at break was 3 % compared to 117 %.

Films of BGE-diol AX0.9 were characterised by a lower modulus (Fig. 4) and a higher strain at break (Table 3). One of the specimens had a strain at break of 50 %, which increased the standard deviation, otherwise the BGE-diol AX0.9 exhibited the highest stretchability of all tested materials. Compared to the BGE-diol AX0.5, the stress-strain curves of BGE-diol AX0.9 were more reminiscent to those of an elastomer (Roberts & Holder, 2011). There was no pronounced necking behavior after the yield point (7–20 % strain), and the strain hardening

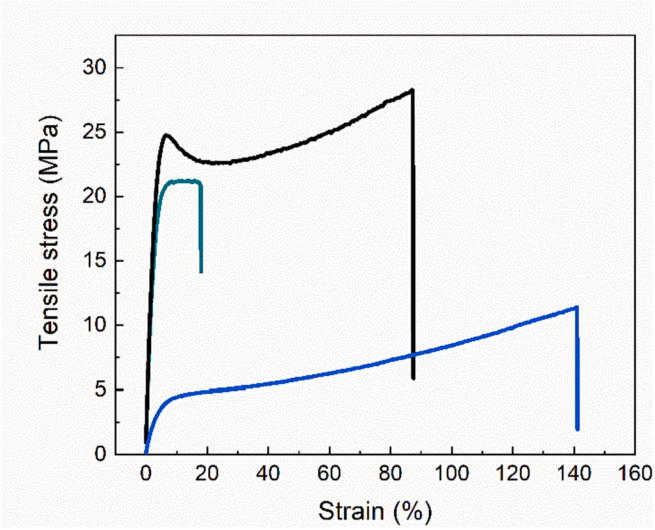

Fig. 4. Stress strain curves of BGE-diol AX0.3 (green), BGE-diol AX0.5 (black), BGE-diol AX0.9 (blue).

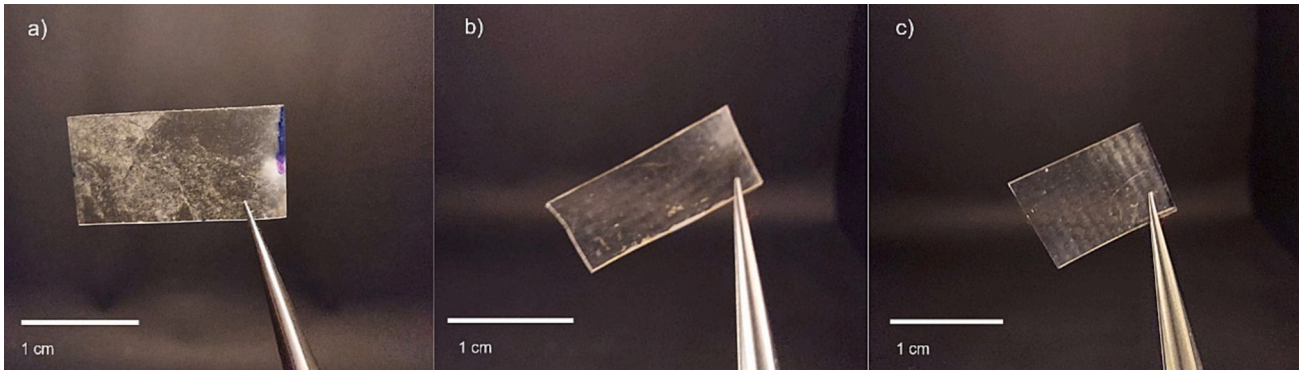

Fig. 3. Images of compression molded films from; a) BGE-diol AX0.3, b) BGE-diol AX0.5, and c) BGE-diol AX0.9, with thickness of 0.1 mm.

Table 3
Tensile properties of compression molded BGE-diol AX films.

Material	Young's modulus (MPa)	Strain at break (%)	Toughness (MJ/m^3)
BGE-diol AX0.3	670 (±130)	15 (±10)	2.7 (±2.8)
BGE-diol AX0.5	740 (±190)	68 (±36)	15.0 (±8.4)
BGE-diol AX0.9	110 (±30)	117(±38)	8.8 (±4.1)

up to failure was relatively low.

Films of BGE-diol AX0.5 had the highest mean tensile toughness at 15 MJ/m^3 (Table 3). They had a Young's modulus close to that of BGE-diol AX0.3, but were more ductile (higher strain at break). As seen in the stress-strain curves: the films of BGE-diol AX0.5 exhibited a clear yield point (at 7 % strain), and a significant strain hardening up to the point of fracture.

Films of BGE-diol AX0.3 were the least ductile of the three modified samples. Several of the tested films underwent failure after yielding, whereas the others could be stretched up to 35 % strain with no necking behavior observed. The low ductility resulted in BGE-diol AX0.3 having the lowest toughness out of the three specimens. The M_w of BGE-diol AX0.3 is similar to that of the BGE-diol AX0.5 (Table 2), therefore the differences in mechanical properties should come from factors other than differences in molar mass. It is possible that macroscopic (Fig. 3a) and microscopic inhomogeneities, discussed in terms of crystallinity in a later section, were acting as fracture points leading to failure.

3.5. Characterization of the polymer structures by X-ray scattering

To understand the changes to the polymer structure after modification, X-ray scattering from two instrument configurations (SAXS and WAXS) were combined to produce the curve in Fig. 5. At low Q (< 0.1 Å^{-1}), steep Q-decays of Q^{-2} for BGE-diol AX0.3, and Q^{-3} for all the other samples were observed. The Q^{-3} decay could be from defects and voids on a nanoscale (Brown, 1987; Paredes & Fischer, 1979; Rottler & Robbins, 2003), occurring from the melt-compression or solvent casting of films. The Q^{-2} decay in the BGE-diol AX0.3 films is expected to be a result of larger structure inhomogeneities, which may be related to the clusters observed macroscopically (Fig. 4a). At 1.5 Å^{-1}, we observed an amorphous peak for all samples, corresponding to an "average" inter-

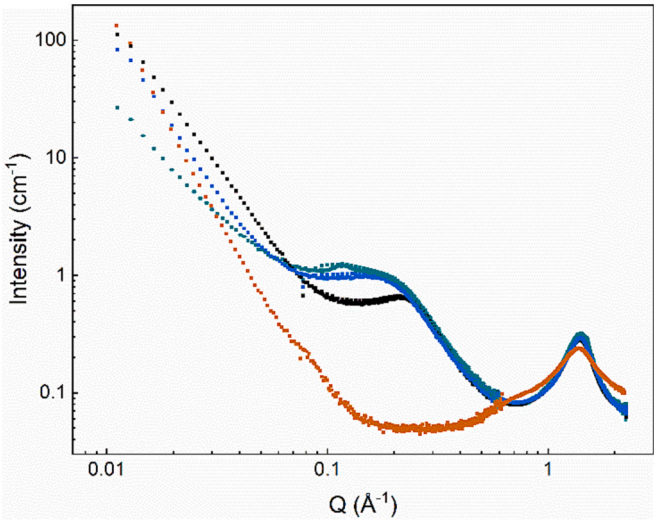

Fig. 5. Combined SAXS and WAXS curve of BGE-diol AX0.3 (green), BGE-diol AX0.5 (black), BGE-diol AX0.9 (blue), and AX0.9 (orange) measured at room temperature.

molecular atom-atom distance. The unmodified AX0.9 has a shoulder at 0.67 Å^{-1}, corresponding to a real space distance of 9.2 Å – calculated from $d = 2\pi/Q$. (Arbe et al., 2008; Beiner & Huth, 2003; Schönhals & Kremer, 2012). The unmodified AX0.9 has a shoulder at 0.67 Å^{-1}, corresponding to a real space distance of 9.2 Å – calculated from $d = 2\pi/Q$. All modified samples showed intense correlation peaks at 0.18 Å^{-1} (BGE-diol AX0.3 and BGE-diol AX0.9) and 0.23 Å^{-1} (BGE-diol AX0.5). These peaks correspond to real space distances of 35 Å and 27 Å, respectively.

The hypothesis is that the space distances originate from aggregation and subsequent nano-domain formation of BGE side chain and AX backbone rich domains respectively. This results in a longer distance between AX backbone chains, thus reducing strong intermolecular interactions between polysaccharide chains. The hypothesis is supported by i) the measured pycnometer density of 1.4 g/cm^3 for AX0.3 and 1.26 g/cm^3 for BGE-diol AX0.3. This indicates that the two nano-domains of BGE side chain and AX would have different mass densities – giving rise to observable X-ray contrast, ii) the AX being more hydrophilic than the hydrophobic BGE, reducing their miscibility and iii) the disappearance of the shoulder observed in unmodified AX0.9 in BGE-diol AX0.9; if the shoulder in AX0.9 originates from the spacing between AX chains caused by arabinose side-groups, then their disappearance and replacement by the larger correlation distance from BGE nano-domains is a reasonable explanation. The reasoning would be in agreement with observations in *comb*-like polymer systems, which showed similar correlation peaks in the 1–5 nm scale: such as poly(n-alkyl methacrylates) (Arbe et al., 2008; Beiner & Huth, 2003), poly(n-alkyl acrylates) (Beiner & Huth, 2003), poly(n-alkylene oxides) (Gerstl et al., 2012), alkyl cellulose (Chen et al., 2014), and alkyl chitosan (Liu et al., 2020).

Native AX0.3 showed Bragg peaks from crystalline chains matching with xylan crystallite diffraction planes in low ara:xyl ratio AX at a Q value of 0.89 Å^{-1} (2θ = 12.4°, 101 & 011), and at a Q value of 1.38 Å^{-1} (2θ = 19.1°, 110) (Fig. S5) (Heikkinen et al., 2013). BGE-diol AX0.3, shows peaks at 1.50 Å^{-1} and 0.12 Å^{-1} in the WAXS curve and at 1.70 Å^{-1} in XRD measurements (Fig. S6) which do not match with those from a xylan crystallite. It was also observed that the peak at 0.12 Å^{-1} becomes more pronounced upon melt compression. The peak at 1.70 Å^{-1} corresponds to a real space distance of 3.7 Å. It could therefore represent small degrees of lateral crystallization within the BGE side chains, The peak centered at 0.12 Å^{-1} represents increased ordering, influenced by a thermal history, with the real space distance of 52 Å suggesting that it is related to an ordering of the nano-domain spacings. The ordered structures formed on the nano-scale, and the macroscopic structures observed through the Q^{-2} decay at low Q for BGE-diol AX0.3, are suggested as explanations for the higher Young's modulus as the ordered structures could hinder the mobility and sliding of the chains under strain. The ordered structures can act as fracture initiation points, leading to the low strain at break observed in tensile testing. Lowered ductility of alkyl celluloses were observed when ordered structures were found in the side chains – the same trend as observed here (Crépy et al., 2011).

No trend could be drawn between the nano-domain size and AX branch density of the materials, BGE-diol AX0.5 had a smaller nano-domain size, but BGE-diol AX0.9 and BGE-diol AX0.3 had similar nano-domain size despite being structurally different (Fig. 1a–c). While the correlation remains unclear, size of the nanodomains do seem to be influenced by the molecular structure of the starting AX. A reference sample of AX0.9 was reacted with a lower amount of BGE without any oxidation-reduction, and a similar correlation peak length to BGE-diol AX0.9 was observed (X-ray curve shown in Fig. S7).

3.6. Temperature step SAXS

Temperature step SAXS curve in Fig. 6a) showed that the correlation peaks exist at higher temperatures. The data also showed a temperature dependence in both Q and intensity of the correlation peaks,

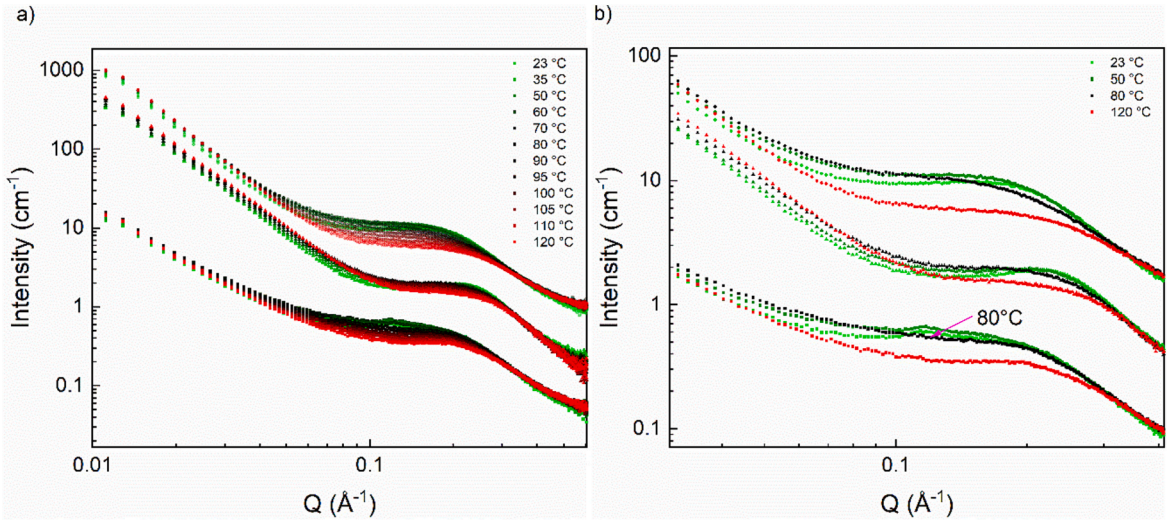

Fig. 6. a) *SAXS* curve, intensity shifted for viewing, as a function of sample temperature from 25 °C (green), to 120 °C (red) for BGE-diol AX0.9 (top), BGE-diol AX0.5 (middle), and BGE-diol AX0.3 (bottom), b) magnification around the shoulder regions. The curve at 80 °C of BGE-diol AX0.3 is indicated by the arrow.

corresponding to fluctuations in size and extent of nano-domains. Fig. 6 shows shoulders that shifted towards lower Q, and increased in intensity between 25 °C and 70 °C. The shift in shoulder and intensity, as a function of temperature, can be explained by swollen nano-domains – likely a result of residual stresses, and moisture effects (between 1 and 2 wt% moisture determined by TGA, Fig. S8). Then, at higher temperatures, the domains shrink again (shifted to higher Q values with decreasing intensity). The BGE-diol AX0.5 correlation peak size remains lower relative to BGE-diol AX0.3 and 0.9 at 120 °C. The decrease in size and intensity at higher temperatures indicates a gradual decrease in order of the hypothesized nano-domains, as a result of increased mobility of both AX and BGE side chains. By the same reasoning, the BGE-diol AX0.5 being less influenced by temperature than the BGE-diol AX0.9 could indicate a lower mobility of the former.

In addition, the disappearance of the sharper peak at 0.12 Å^{-1} for BGE-diol AX0.3 was observed between the 70 °C and 80 °C curve in Fig. 6b). The disappearance of the peak at 0.12 Å^{-1} supports the hypothesis of ordered structure being formed within the sample.

3.7. Thermal properties

DMA data for BGE-diol AX samples are shown in Fig. 7a–c. As shown in the loss modulus (E") and damping (tan delta) curves, three different transitions were observed. We refer to them here as the γ, ß and α transitions, in order of increasing temperature. The γ transition occurred at ca. -90 °C and resulted in a substantial decrease in storage modulus (E'). The β transition occurred at ca. -50 °C for BGE-diol AX0.3 and BGE-diol AX0.9 and at a somewhat higher temperature for BGE-diol AX0.5 (ca. -30 °C). This was also accompanied by a substantial decrease in E'. The third (α) transition was observed as a peak in E" at approx. 70, 75 and 80 °C for BGE-diol AX0.9, BGE-diol AX0.3 and BGE-diol AX0.5 respectively. Beyond this transition both E' and E" decreased drastically. Above the α transition it was possible to compression mold the sample, consequently, we consider the α transition to be the (main) glass transition.

The results reported in this work, and in previous work (Deralia et al., 2022), indicate that the addition of BGE creates transitions below 0 °C due to the molecular flexibility induced by the side chain. The β transition is therefore likely attributed to the relaxation of the side chains. This is also in agreement with works on cellulose esters (Crépy et al., 2011) and glucomannan esters (Enomoto-Rogers et al., 2014) where a relaxation around −60 °C was observed. However, the presence of a γ transition in our systems suggests that BGE-diol AX sidechains contribute with additional/specific modes of movement, such as rotations around the ether bond in the middle of the BGE side chain. The α transition is probably attributed to relaxations of the AX main chain, similar to that of cellulose esters (Crépy et al., 2011).

The DSC plots indicated a weak transition around −50 °C (somewhat higher temperature for BGE-diol AX0.5), and all BGE-diol samples showed a broad transition around 90 °C (Fig. 8). The unmodified AX sample did not show any observable transitions within the same temperature range. The broadness and low intensity of the transitions was expected based on the work on cellulose and xylan esters (Crépy et al., 2011; Fundador et al., 2012). However, the temperature positions of the DSC measured transitions were in fair agreement to those obtained with DMA.

Hiller et al. (2004) described dynamics within branched nanophase separated poly (n-alkyl acrylates) as exhibiting two T_g: a lower $T_{g,\ side\ chain}$ and a higher $T_{g,\ \alpha}$ of the entire chain. Between $T_{g,\ side\ chain} < T < T_{g,\ \alpha}$, the polymer exhibits some mobility, but the modulus is kept relatively high by the rigidity of the main chains separating the mobile alkyl domains. The alkyl domains in poly (n-alkyl acrylates) also serve as a form of internal plasticization, bringing $T_{g,\ \alpha}$ down as well (Hiller et al., 2004). Based on structural X-ray data observed for BGE-diol AX samples, as well as DMA and DSC data, the same type of behavior could be reasoned. The BGE chains separate the AX backbone, reducing strong intermolecular bonding between AX chains, resulting in two dynamics existing in the system. The ß and α-transitions measured in DMA then correspond to $T_{g,\ side\ chain}$ and $T_{g,\ \alpha}$ respectively.

The Young's modulus and tensile ductility are affected by both the side chains and the structure of the native AX that acts as the backbone. It is known that adding more BGE would improve the flexibility of the material. In our study, we show that the branching ratio of the starting AX also has a significant effect on the flexibility of the material. In the case of BGE-diol AX0.3, X-ray scattering as well as macroscopic inhomogeneities suggest that it is the formation of ordered structures at different length scales, which result in their higher stiffness and lower strain at break. For BGE-diol AX0.5, we observed smaller nano-domain sizes and a lower response to temperature increases through SAXS/WAXS. In addition, the ß-transition in DMA, which has the largest effect on E' at room temperature, was observed at a higher temperature (−30 °C compared to −50 °C in BGE-diol AX0.9) and with lower relative intensity to the γ-transition (−90 °C). Both SAXS/WAXS and DMA data therefore suggest that side chain domain related relaxation behavior is hindered in BGE-diol AX0.5. It is unclear why this particular AX structure produces these results. However, the observations could reasonably

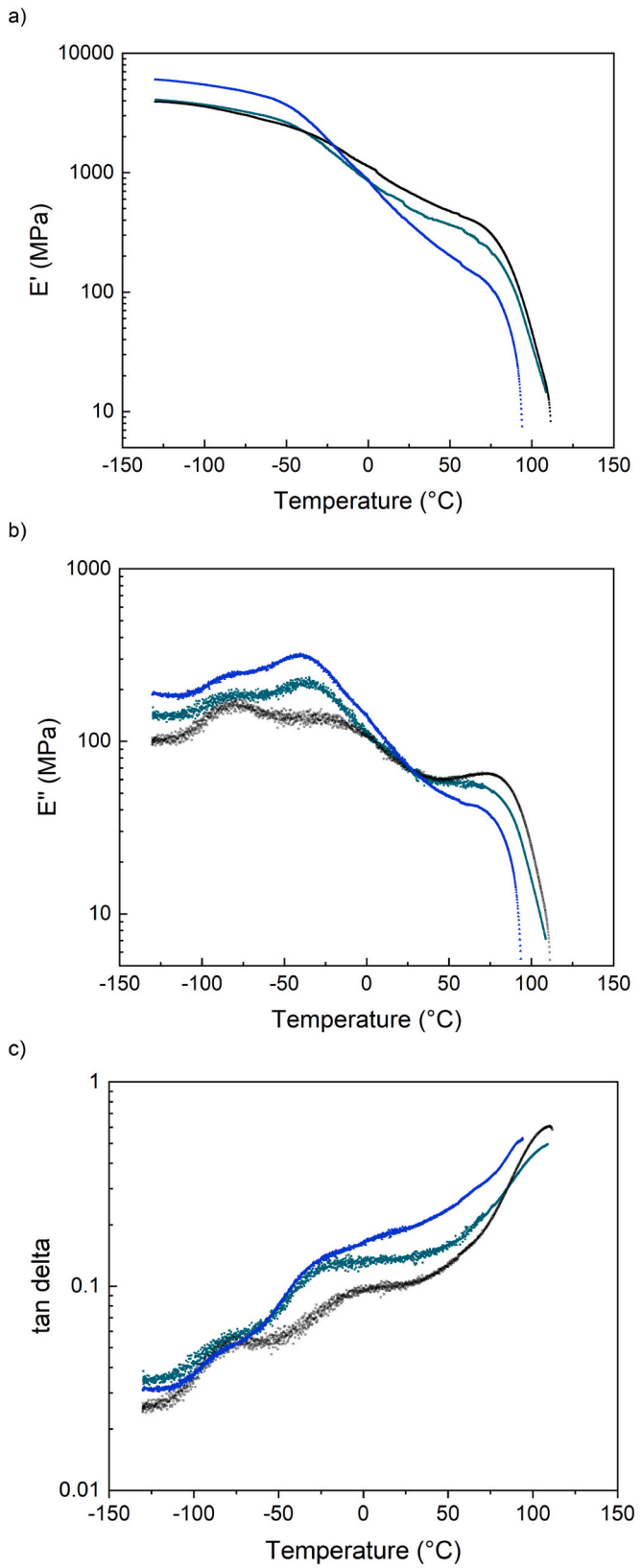

Fig. 7. DMA curves of BGE-diol AX 0.3 (green), BGE-diol AX0.5 (black), BGE-diol AX0.9 (blue): a) E', b) E", and c) the tan delta as a function of temperature. Measurements performed at frequency of 1 Hz and strain amplitude of 8 μm.

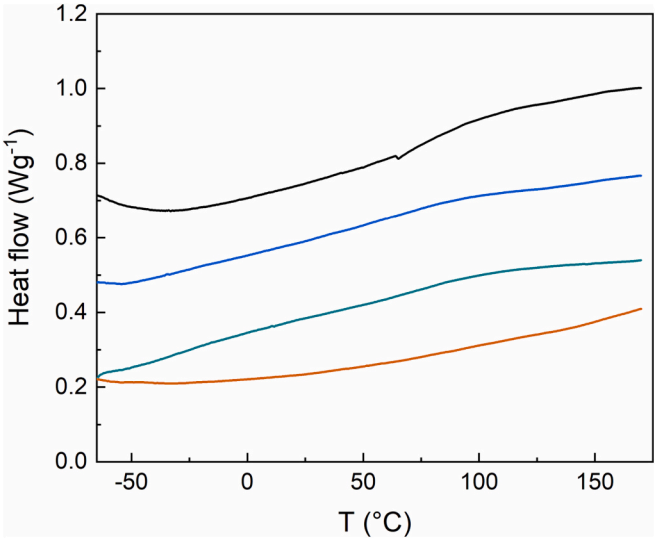

Fig. 8. Second heating DSC curves for AX0.9 (orange), BGE-diol AX0.3 (green), BGE-diol AX0.5 (black), BGE-diol AX0.9 (blue). Endothermal direction is upwards.

be correlated to the BGE-diol AX0.5's highest modulus at room temperature of all modified AX materials.

Stepan et al. (2012) observed similar trends in Young's modulus and ductility in acetylated arabinoxylan films, although the differences were not as large. Acetyl groups are shorter than BGE side chains, which could explain the differences observed.

4. Conclusions

The diffusivity, measured by pulsed-field gradient NMR, corroborates the effective reaction of BGE on oxidized and reduced AX, where no or little BGE exist unreacted. A comparison of three fractions of wheat bran AX with different arabinose content were made with regards to the final material thermomechanical properties after oxidation-reduction-etherification modification. We obtained melt processable materials independent of initial arabinose content at similar MS. A significant difference in Young's modulus and ductility of compression molded films were observed, with higher arabinose contents associated with a more ductile modified material. The hypothesized model for the behavior exhibited by the system is that of a nanophase separated system consisting of more mobile side chain domains surrounded by the rigid AX main chains. The presence of ordered structures, size of side chain nano-domains and temperature response of the nano-domains were found to be correlated to the starting AX material properties. The findings provide insight on how chemical modification may turn an unmelt-processable polysaccharide into a thermoplastic material and shows that the mechanical properties of the final product can be tuned by controlling the composition of the polysaccharide starting material.

Funding sources

Formas – a Swedish Research Council for Sustainable Development, with grant number 2020–01235 and Lantmännen foundation, grant number 2020H064.

CRediT authorship contribution statement

Ratchawit Janewithayapun: Conceptualization, Investigation, Methodology, Visualization, Writing – original draft. **Mikael S. Hedenqvist:** Supervision, Validation, Writing – review & editing. **Fabrice Cousin:** Supervision, Validation, Writing – review & editing.

Alexander Idström: Investigation, Writing – original draft. **Lars Evenäs:** Formal analysis, Writing – review & editing. **Patricia Lopez Sanchez:** Investigation, Writing – review & editing. **Gunnar Westman:** Resources, Writing – review & editing. **Anette Larsson:** Supervision, Validation, Writing – review & editing. **Anna Ström:** Conceptualization, Funding acquisition, Supervision, Writing – review & editing.

Declaration of competing interest

The authors declare the following financial interests/personal relationships which may be considered as potential competing interests: Ratchawit Janewithayapun reports financial support was provided by Swedish Research Council Formas. If there are other authors, they declare that they have no known competing financial interests or personal relationships that could have appeared to influence the work reported in this paper.

Data availability

Data will be made available on request.

Acknowledgment

We would like to acknowledge the Chalmers Material Analysis Laboratory for access to X-ray scattering and diffraction instruments, and the research engineer Michal Strach for his help with training and instrument setup. We would also like to acknowledge the Division of Forest Products and Chemical Engineering at Chalmers for access to monosaccharide analysis instruments. Lastly, we are grateful for financial support from Formas – a Swedish Research Council for Sustainable Development, with grant number 2020-01235 and the Lantmännen foundation, grant number 2020H064.

Appendix A. Supplementary data

Additional data on FTIR, 1H diffusion NMR, tensile tests, X-ray scattering and TGA for other selected samples (supplementary.docx). Supplementary data to this article can be found online at doi:https://doi.org/10.1016/j.carbpol.2024.121846.

References

Amer, H., Nypelö, T., Sulaeva, I., Bacher, M., Henniges, U., Potthast, A., & Rosenau, T. (2016). Synthesis and characterization of Periodate-oxidized polysaccharides: Dialdehyde Xylan (DAX). *Biomacromolecules, 17*(9), 2972–2980. https://doi.org/10.1021/acs.biomac.6b00777

Arbe, A., Genix, A. C., Colmenero, J., Richter, D., & Fouquet, P. (2008). Anomalous relaxation of self-assembled alkyl nanodomains in high-order poly(n-alkyl methacrylates) [10.1039/B807192F]. *Soft Matter, 4*(9), 1792–1795. https://doi.org/10.1039/B807192F

Beiner, M., & Huth, H. (2003). Nanophase separation and hindered glass transition in side-chain polymers. *Nature Materials, 2*(9), 595–599. https://doi.org/10.1038/nmat966

Börjesson, M., Larsson, A., Westman, G., & Ström, A. (2018a). Periodate oxidation of xylan-based hemicelluloses and its effect on their thermal properties. *Carbohydrate Polymers, 202*, 280–287. https://doi.org/10.1016/j.carbpol.2018.08.110

Börjesson, M., Larsson, A., Westman, G., & Ström, A. (2018b). *A process for preparing modified hemicellulose* EP3700941A1·2020-09-02. E. P. *Office*, 18–24. https://worldwide.espacenet.com/patent/search?q=pn%3DEP3700941A1.

Börjesson, M., Westman, G., Larsson, A., & Ström, A. (2019). Thermoplastic and flexible films from Arabinoxylan. *ACS Applied Polymer Materials, 1*(6), 1443–1450. https://doi.org/10.1021/acsapm.9b00205

Brown, H. R. (1987). Polymer degradation by crazing and its study by small angle scattering techniques. *Materials Science Reports, 2*(6), 317–370. https://doi.org/10.1016/S0920-2307(87)80006-3

Chen, X., Zheng, N., Wang, Q., Liu, L., & Men, Y. (2014). Effect of synthetic pathways on the phase transition and side-chain crystallization behavior of alkyl-substituted cellulose ethers [10.1039/C4PY00394B]. *Polymer Chemistry, 5*(13), 4105–4114. https://doi.org/10.1039/C4PY00394B

Cheng, K., Zhou, Y., & Neelamegham, S. (2016). DrawGlycan-SNFG: A robust tool to render glycans and glycopeptides with fragmentation information. *Glycobiology, 27*(3), 200–205. https://doi.org/10.1093/glycob/cww115

Crépy, L., Miri, V., Joly, N., Martin, P., & Lefebvre, J.-M. (2011). Effect of side chain length on structure and thermomechanical properties of fully substituted cellulose fatty esters. *Carbohydrate Polymers, 83*(4), 1812–1820. https://doi.org/10.1016/j.carbpol.2010.10.045

De Man, W. L., Vaneeckhaute, E., De Brier, N., Wouters, A. G. B., Martens, J. A., Breynaert, E., & Delcour, J. A. (2021). 1H diffusion-ordered nuclear magnetic resonance spectroscopic analysis of water-extractable Arabinoxylan in wheat (Triticum aestivum L.). *Flour. Journal of Agricultural and Food Chemistry, 69*(13), 3912–3922. https://doi.org/10.1021/acs.jafc.1c00180

Deralia, P. K., du Poset, A. M., Lund, A., Larsson, A., Ström, A., & Westman, G. (2021a). Hydrophobization of arabinoxylan with n-butyl glycidyl ether yields stretchable thermoplastic materials. *International Journal of Biological Macromolecules, 188*, 491–500. https://doi.org/10.1016/j.ijbiomac.2021.08.041

Deralia, P. K., du Poset, A. M., Lund, A., Larsson, A., Ström, A., & Westman, G. (2021b). Oxidation level and Glycidyl ether structure determine thermal Processability and thermomechanical properties of Arabinoxylan-derived thermoplastics. *ACS Applied Bio Materials, 4*(4), 3133–3144. https://doi.org/10.1021/acsabm.0c01550

Deralia, P. K., Sonker, A. K., Lund, A., Larsson, A., Ström, A., & Westman, G. (2022). Side chains affect the melt processing and stretchability of arabinoxylan biomass-based thermoplastic films. *Chemosphere, 294*, Article 133618. https://doi.org/10.1016/j.chemosphere.2022.133618

Enomoto-Rogers, Y., Ohmomo, Y., Takemura, A., & Iwata, T. (2014). Syntheses of glucomannan esters and their thermal and mechanical properties. *Carbohydrate Polymers, 101*, 592–599. https://doi.org/10.1016/j.carbpol.2013.09.103

Farhat, W., Venditti, R., Ayoub, A., Prochazka, F., Fernández-de-Alba, C., Mignard, N., Taha, M., & Becquart, F. (2018). Towards thermoplastic hemicellulose: Chemistry and characteristics of poly-(ε-caprolactone) grafting onto hemicellulose backbones. *Materials & Design, 153*, 298–307. https://doi.org/10.1016/j.matdes.2018.05.013

Fundador, N. G. V., Enomoto-Rogers, Y., Takemura, A., & Iwata, T. (2012). Syntheses and characterization of xylan esters. *Polymer, 53*(18), 3885–3893. https://doi.org/10.1016/j.polymer.2012.06.038

Gerstl, C., Brodeck, M., Schneider, G. J., Su, Y., Allgaier, J., Arbe, A., … Richter, D. (2012). Short and intermediate range order in poly(alkylene oxide)s. a neutron diffraction and molecular dynamics simulation study. *Macromolecules, 45*(17), 7293–7303. https://doi.org/10.1021/ma301197y

Heikkinen, S. L., Mikkonen, K. S., Pirkkalainen, K., Serimaa, R., Joly, C., & Tenkanen, M. (2013). Specific enzymatic tailoring of wheat arabinoxylan reveals the role of substitution on xylan film properties. *Carbohydrate Polymers, 92*(1), 733–740. https://doi.org/10.1016/j.carbpol.2012.09.085

Hiller, S., Pascui, O., Budde, H., Kabisch, O., Reichert, D., & Beiner, M. (2004). Nanophase separation in side chain polymers: New evidence from structure and dynamics. *New Journal of Physics, 6*(1), 10. https://doi.org/10.1088/1367-2630/6/1/010

Jedvert, K., Saltberg, A., Theliander, H., Wang, Y., Henriksson, G., & Lindström, M. E. (2012). Mild steam explosion: A way to activate wood for enzymatic treatment, chemical pulping and biorefinery processes. *BIOREFINERY, 27*(5), 828–835. https://doi.org/10.3183/npprj-2012-27-05-p828-835 (Nordic Pulp & Paper Research Journal)

Jia, S., Lv, Z., Rao, J., Lü, B., Chen, G., Bian, J., … Peng, F. (2023). Xylan plastic. *ACS Nano, 17*(14), 13627–13637. https://doi.org/10.1021/acsnano.3c02327

Kristiansen, K. A., Potthast, A., & Christensen, B. E. (2010). Periodate oxidation of polysaccharides for modification of chemical and physical properties. *Carbohydrate Research, 345*(10), 1264–1271. https://doi.org/10.1016/j.carres.2010.02.011

Landel, R. F., & Nielsen, L. E. (1993). *Mechanical properties of polymers and composites* (2nd ed.). CRC Press. https://doi.org/10.1201/b16929

Larsson, P. A., Berglund, L. A., & Wågberg, L. (2014). Ductile All-Cellulose Nanocomposite Films Fabricated from Core–Shell Structured Cellulose Nanofibrils. Biomacromolecules, 15(6), 2218–2223. doi:https://doi.org/10.1021/bm500360c.

Liu, L., Lyu, D., Xiang, M., & Men, Y. (2020). Side chain packing states of chitosan-based supramolecular derivatives containing long alkyl side chains. *POLYMER CRYSTALLIZATION, 3*(2), Article e10110. https://doi.org/10.1002/pcr2.10110

Maekawa, E., Kosaki, T., & Koshijima, T. (1986). Periodate oxidation of mercerized cellulose and regenerated cellulose. *Wood research: bulletin of the Wood Research Institute Kyoto University, 73*, 44–49.

Maes, C., & Delcour, J. A. (2002). Structural characterisation of water-extractable and water-unextractable Arabinoxylans in wheat bran. *Journal of Cereal Science, 35*(3), 315–326. https://doi.org/10.1006/jcrs.2001.0439

Nylander, F., Svensson, O., Josefson, M., Larsson, A., & Westman, G. (2019). New features of arabinoxylan ethers revealed by using multivariate analysis. *Carbohydrate Polymers, 204*, 255–261. https://doi.org/10.1016/j.carbpol.2018.09.062

Nypelö, T., Laine, C., Aoki, M., Tammelin, T., & Henniges, U. (2016). Etherification of wood-based hemicelluloses for interfacial activity. *Biomacromolecules, 17*(5), 1894–1901. https://doi.org/10.1021/acs.biomac.6b00355

Nypelö, T., Rogers, S., Ström, A., Cavalcanti, L. P., Palasingh, C., & Janewithayapun, R. (2022). *Physico-chemical properties of xylans (RB2220239)*. https://doi.org/10.5286/ISIS.E.RB2220239

Palasingh, C., Nakayama, K., Abik, F., Mikkonen, K. S., Evenäs, L., Ström, A., & Nypelö, T. (2022). Modification of xylan via an oxidation–reduction reaction. *Carbohydrate Polymers, 292*, Article 119660. https://doi.org/10.1016/j.carbpol.2022.119660

Paredes, E., & Fischer, E. W. (1979). Röntgenkleinwinkel-untersuchungen zur struktur der crazes (fließzonen) in polycarbonat und polymethylmethacrylat. *Die Makromolekulare Chemie, 180*(11), 2707–2722. https://doi.org/10.1002/macp.1979.021801112

Petermann, M., Dianteill, L., Zeidi, A., Vaha Ouloassekpa, R., Budisavljevic, P., Le Men, C., … Bouchoux, A. (2023). Arabinoxylan in water through SANS: Single-chain

conformation, chain overlap, and clustering. *Biomacromolecules, 24*(8), 3619–3628. https://doi.org/10.1021/acs.biomac.3c00374

Prückler, M., Siebenhandl-Ehn, S., Apprich, S., Höltinger, S., Haas, C., Schmid, E., & Kneifel, W. (2014). Wheat bran-based biorefinery 1: Composition of wheat bran and strategies of functionalization. *LWT - Food Science and Technology, 56*(2), 211–221. https://doi.org/10.1016/j.lwt.2013.12.004

Roberts, D. R. T., & Holder, S. J. (2011). Mechanochromic systems for the detection of stress, strain and deformation in polymeric materials [10.1039/C0JM04237D]. *Journal of Materials Chemistry, 21*(23), 8256–8268. https://doi.org/10.1039/C0JM04237D

Rottler, J., & Robbins, M. O. (2003). Growth, microstructure, and failure of crazes in glassy polymers. *Physical Review E, 68*(1), Article 011801. https://doi.org/10.1103/PhysRevE.68.011801

Schönhals, A., & Kremer, F. (2012). 1.08 - amorphous polymers. In K. Matyjaszewski, & M. Möller (Eds.), *Polymer science: A comprehensive reference* (pp. 201–226). Elsevier. https://doi.org/10.1016/B978-0-444-53349-4.00010-8.

Sluiter, A., Hames, B., Ruiz, R., Scarlata, C., Sluiter, J., Templeton, D., & Crocker, D. (2008). Determination of structural carbohydrates and lignin in biomass. *Laboratory analytical procedure, 1617*(1), 1–16.

Stepan, A. M., Höije, A., Schols, H. A., de Waard, P., & Gatenholm, P. (2012). Arabinose content of arabinoxylans contributes to flexibility of acetylated arabinoxylan films. *Journal of Applied Polymer Science, 125*(3), 2348–2355. https://doi.org/10.1002/app.36458

Theander, O., & Westerlund, E. A. (1986). Studies on dietary fiber. 3. Improved procedures for analysis of dietary fiber. *Journal of Agricultural and Food Chemistry, 34*(2), 330–336. https://doi.org/10.1021/jf00068a045

Verwimp, T., Van Craeyveld, V., Courtin, C. M., & Delcour, J. A. (2007). Variability in the structure of Rye flour alkali-extractable Arabinoxylans. *Journal of Agricultural and Food Chemistry, 55*(5), 1985–1992. https://doi.org/10.1021/jf0623790